

# Geophysical Research Letters



## RESEARCH LETTER

10.1029/2019GL083613

### Key Points:

- Al substitution in bridgmanite is dominated by the oxygen vacancy mechanism for peridotite mantle compositions
- Short-range ordering of oxygen vacancies takes place forming oxygen vacancy clusters possibly due to migration into twin domain walls
- Oxygen vacancy clusters are expected to have a major influence on transport properties of the lower mantle, such as the electrical conductivity

### Supporting Information:

- Supporting Information S1
- Data Set S1

### Correspondence to:

J. Senker, and D. J. Frost,  
dan.frost@uni-bayreuth.de  
juergen.senker@uni-bayreuth.de

### Citation:

Grüninger, H., Liu, Z., Siegel, R., Boffa Ballaran, T., Katsura, T., Senker, J., & Frost, D. J. (2019). Oxygen vacancy ordering in aluminous bridgmanite in the Earth's lower mantle. *Geophysical Research Letters*, 46, 8731–8740. <https://doi.org/10.1029/2019GL083613>

Received 6 MAY 2019

Accepted 8 JUL 2019

Accepted article online 19 JUL 2019

Published online 5 AUG 2019

The copyright line for this article was changed on 13 AUG 2019 after original online publication.

©2019. The Authors.

This is an open access article under the terms of the Creative Commons Attribution-NonCommercial-NoDerivs License, which permits use and distribution in any medium, provided the original work is properly cited, the use is non-commercial and no modifications or adaptations are made.

## Oxygen Vacancy Ordering in Aluminous Bridgmanite in the Earth's Lower Mantle

Helen Grüninger<sup>1</sup> , Zhaodong Liu<sup>2</sup> , Renée Siegel<sup>1</sup>, Tiziana Boffa Ballaran<sup>2</sup> , Tomoo Katsura<sup>2</sup> , Jürgen Senker<sup>1</sup> , and Daniel J. Frost<sup>2</sup> 

<sup>1</sup>Inorganic Chemistry III, University of Bayreuth, Bayreuth, Germany, <sup>2</sup>Bayerisches Geoinstitut, University of Bayreuth, Bayreuth, Germany

**Abstract** Oxygen vacancies (OVs), that charge-balance the replacement of octahedrally coordinated Si<sup>4+</sup> by Al<sup>3+</sup> in the mineral bridgmanite, will influence transport properties in the lower mantle but little is known about their stability and local structure. Using <sup>27</sup>Al nuclear magnetic resonance (NMR) spectroscopy we have characterized OVs within six aluminous bridgmanite samples. In the resulting NMR spectra sixfold, fivefold, and fourfold coordinated Al species are resolved, in addition to near eightfold coordinated Al substituting for Mg. Fivefold coordinated Al is formed by single OV sites but fourfold coordination must result from short range ordering of OVs, producing OV clusters that may form through migration into twin domain walls. Characterizing the occurrence of such OV structures is an important prerequisite for understanding how transport properties change with depth and composition in the lower mantle.

**Plain Language Summary** The lower mantle encompasses the largest region of the Earth's interior and is mainly composed of the perovskite-structured mineral (Mg,Fe,Al)(Al,Si)O<sub>3</sub> bridgmanite. Its properties, therefore, control both the diffusive transport of elements and solid state flow in the lower mantle, which will be strongly influenced by point defects. We have identified and quantified defects in bridgmanite that arise from the replacement of silicon by aluminum and result in the creation of a vacant oxygen site. These oxygen defects are also found to form clusters in the structure, which in other perovskite structured minerals have been shown to strongly affect physical properties. As defect formation and ordering is dependent on composition and pressure, strong variations in physical properties may be expected within the upper 300 km of the lower mantle.

### 1. Introduction

In order to understand transport properties such as creep and electrical conductivity in the lower mantle, it is important to characterize the nature of the determinant point defects in the dominant lower mantle mineral bridgmanite, which occur mainly as a result of the substitution of trivalent cations (Kurnosov et al., 2017; Manthilake et al., 2011; McCammon, 1997; Navrotsky, 1999; Xu & McCammon, 2002). Perovskite structured MgSiO<sub>3</sub> bridgmanite contains Si in octahedral coordination (B site substitution) and Mg occupying a larger dodecahedral site (A site substitution). Al is the most abundant trivalent cation substituting into bridgmanite, followed by Fe<sup>3+</sup> (Lauterbach et al., 2000; McCammon, 1997), and can be incorporated either by substituting for Si, with charge balance provided through the formation of oxygen vacancies (OVs), or by the coupled substitution of Mg and Si by 2 Al. The former mechanism is characterized by the fictive end-member MgAlO<sub>2.5</sub> and is expected to be favored in bulk pyrolytic mantle compositions where the presence of ferropericlase, (Mg,Fe)O renders a low silica activity (Brodholt, 2000; Navrotsky, 1999). The latter charge coupled (CC) mechanism should be dominant in Al<sub>2</sub>O<sub>3</sub>- or SiO<sub>2</sub>-rich systems as well as in the deeper portions of the lower mantle (Brodholt, 2000; Liu, Ishii, et al., 2017; Liu, Nishi, et al., 2017). The two mechanisms should have different impacts on the elastic properties, diffusivity, conductivity, and rheology of bridgmanite. Oxygen mobility in ceramic perovskites studied for fuel cell applications, for example, has been shown to be controlled by the concentration of OVs (Navrotsky, 1999) and the mobility of protons in bridgmanite may be similarly controlled, even if the absolute solubility remains low (Bolfan-Casanova et al., 2000; Navrotsky et al., 2003). As in ceramic perovskites, changes in the transport properties of bridgmanite will likely also depend on the local distribution of OVs in the structure (Klie et al., 2001; Kruidhof et al., 1993). In many perovskites progressive ordering of OVs occurs with increasing trivalent cation substitution, from locally ordered dimer and trimer clusters to extended chains and ultimately to planes with long range

ordering, such as in the end member  $\text{Ca}(\text{Al,Fe})\text{O}_{2.5}$  brownmillerite (Becerro et al., 1999). Changes in OV ordering are also linked to changes in transport properties such as electrical conductivity and oxygen diffusivity (Figueiredo et al., 2003; Zhang & Smyth, 1995). To date, however, no evidence for OV ordering in bridgmanite has been reported and even the occurrence of OVs has been mainly implied through chemical analyses. X-ray absorption and nuclear magnetic resonance (NMR) spectroscopic studies of the local structure around the Al atoms in bridgmanite have identified Al in sixfold or higher coordination (Andrault et al., 1998; Palke et al., 2012; Stebbins et al., 2001, 2003), consistent with the CC mechanism, although Stebbins et al. (2006) observed an Al B to A ratio of 2:1 in one sample of bridgmanite from which the formation of OVs was implied.

Recent high pressure experiments, which have used chemical compositions to infer the existence of OVs in Al-bearing bridgmanite, imply that they are stabilized in MgO-saturated bulk compositions with increasing temperature (Liu et al., 2019) but decrease in abundance with both increasing Al contents ( $>0.1$  Al atoms per  $\text{MgSiO}_3$  formula unit, henceforth, pfu) and pressure (Liu, Ishii, & Katsura, 2017; Liu, Nishi, et al., 2017). Although these conditions are consistent with OVs being important at the top of the lower mantle and are likely to be the most abundant type of vacancy defect in the entire mantle, the conditions where the OV mechanism dominates over the CC mechanism are sensitive to the pressure, temperature, and chemical composition and have likely been overlooked in many previous experimental studies.

Here we report the first detection of ordering of OVs in Al-bearing bridgmanite using an analysis of  $^{27}\text{Al}$  magic angle spinning (MAS) NMR spectra. A suit of bridgmanite samples were synthesized over a range of Al contents and  $\text{SiO}_2$  activities designed to explore the extent of OV formation. To clarify the type and ratio of the Al species within bridgmanite, density functional theory (DFT) calculations for various CC and OV defect configurations were combined with a quantitative analysis of  $^{27}\text{Al}$  MAS NMR spectra for all samples. For the interpretation of the  $^{27}\text{Al}$  NMR spectra we rely on identifying the characteristic lineshapes for the Al species based on reference spectra where the different Al substitution mechanisms, OV and CC are at a maximum. Two-dimensional  $^{27}\text{Al}$  satellite-transition MAS (STMAS) NMR spectroscopy was also employed to increase the spectral resolution. We provide direct evidence for the formation of OVs, their concentration, and ordering as a function of bridgmanite composition and show that they should dominate the Al substitution mechanism in the upper region of the lower mantle and thereby exert an important influence on transport properties.

## 2. Materials and Methods

Six Al-bearing bridgmanite samples were investigated in this study: three samples were synthesized along the join  $\text{MgSiO}_3\text{-MgAlO}_{2.5}$  and two along the join  $\text{MgSiO}_3\text{-Al}_2\text{O}_3$  (Table 1) using a multianvil apparatus (Ishii et al., 2016). To ensure chemical homogeneity, vitreous (glassed) starting materials were employed. A further bridgmanite sample was synthesized from a starting material composed of 70 wt% of enstatite containing 5 mol% of  $\text{Al}_2\text{O}_3$  and 30 wt% of MgO (sample F). All samples were recovered from the high-pressure high-temperature runs in the form of well-sintered pellets, which were analyzed without being ground to a powder in order to avoid amorphization.

Characterization was performed by means of scanning electron microscopy (Figure S1 in the supporting information) and powder X-ray diffraction (Figure 1). The samples comprised either monomineralic bridgmanite or bridgmanite plus MgO or  $\text{Al}_2\text{O}_3$  (Table 1). The proportions of the stoichiometric CC and OV components present in the synthesized Al-bearing bridgmanites (Table 1) were estimated from their compositions, as measured by electron probe microanalyzer (EPMA, Table S3), according to the following expression:



Quantitative 1-D  $^{27}\text{Al}$  MAS NMR spectra (Kentgens, 1991) were acquired to probe the local Al environment within bridgmanite (Figure 1). Furthermore, for sample B a 2-D  $^{27}\text{Al}$  STMAS spectrum (Kwak & Gan, 2003; Siegel et al., 2009) was recorded to enhance the resolution and to identify the spectral lineshape of the individual Al defect sites (Figure 2). One-dimensional  $^{27}\text{Al}$  MAS NMR echo spectra of sample A and B were recorded at a higher magnetic field of 23.5 T (Figure S4) to corroborate the results of the quantitative analysis. DFT calculations of multiple Al defect structures were used to determine the expected NMR parameters

**Table 1**  
Al-Bearing Bridgmanite Samples Investigated in This Study

Starting materials	Synthesised products	Brg compositions	OV (mol%)	CC (mol%)
A (En <sub>95</sub> Brm <sub>5</sub> )	Brg	Mg <sub>0.991</sub> Al <sub>0.050</sub> Si <sub>0.959</sub> O <sub>2.984</sub>	3.2 (9)	0.9 (1)
B (En <sub>90</sub> Brm <sub>10</sub> )	Brg	Mg <sub>0.975</sub> Al <sub>0.100</sub> Si <sub>0.925</sub> O <sub>2.975</sub>	5.0 (8)	2.5 (5)
C (En <sub>80</sub> Brm <sub>20</sub> )	Brg + Per	Mg <sub>0.937</sub> Al <sub>0.161</sub> Si <sub>0.902</sub> O <sub>2.982</sub>	3.5 (7)	6.3 (4)
D (En <sub>95</sub> Cor <sub>5</sub> )	Brg	Mg <sub>0.952</sub> Al <sub>0.101</sub> Si <sub>0.947</sub> O <sub>2.998</sub>	0.5 (8)	4.8 (3)
E (En <sub>75</sub> Cor <sub>25</sub> )	Brg + Cor + trace Sti	Mg <sub>0.884</sub> Al <sub>0.235</sub> Si <sub>0.881</sub> O <sub>2.999</sub>	0.3 (7)	11.6 (4)
F <sup>a</sup>	Brg + Per	Mg <sub>0.968</sub> Al <sub>0.099</sub> Si <sub>0.933</sub> O <sub>2.983</sub>	3.5 (9)	3.2 (6)

Note. Uncertainties on oxygen vacancy (OV) and charge coupled (CC) contents are calculated from the microprobe analysis uncertainties reported in Table S3. Brm = MgAlO<sub>2.5</sub> (brownmillerite); Brg = bridgmanite; Cor = Al<sub>2</sub>O<sub>3</sub>; En = MgSiO<sub>3</sub>; Per = periclase; Sti = stishovite.

<sup>a</sup>The F starting material consisted of a mixture of 70 wt.% enstatite synthesized from glass D and 30 wt.% MgO.

for different scenarios of the CC and OV substitution mechanism. The simulations were carried out using the CASTEP DFT code (Charpentier, 2011; Clark et al., 2005; Grimme, 2006; Perdew et al., 1996; Pickard & Mauri, 2001; Profeta et al., 2003; Yates et al., 2007). Details on synthesis conditions, DFT calculations, and characterization methods are summarized in the supporting information.

### 3. Results

<sup>27</sup>Al MAS NMR spectra were collected on six Al-bearing bridgmanite samples (A to F; Figure 1). All spectra show a sharp resonance at ~7 ppm, corresponding to Al in a symmetric octahedral environment, and a broad

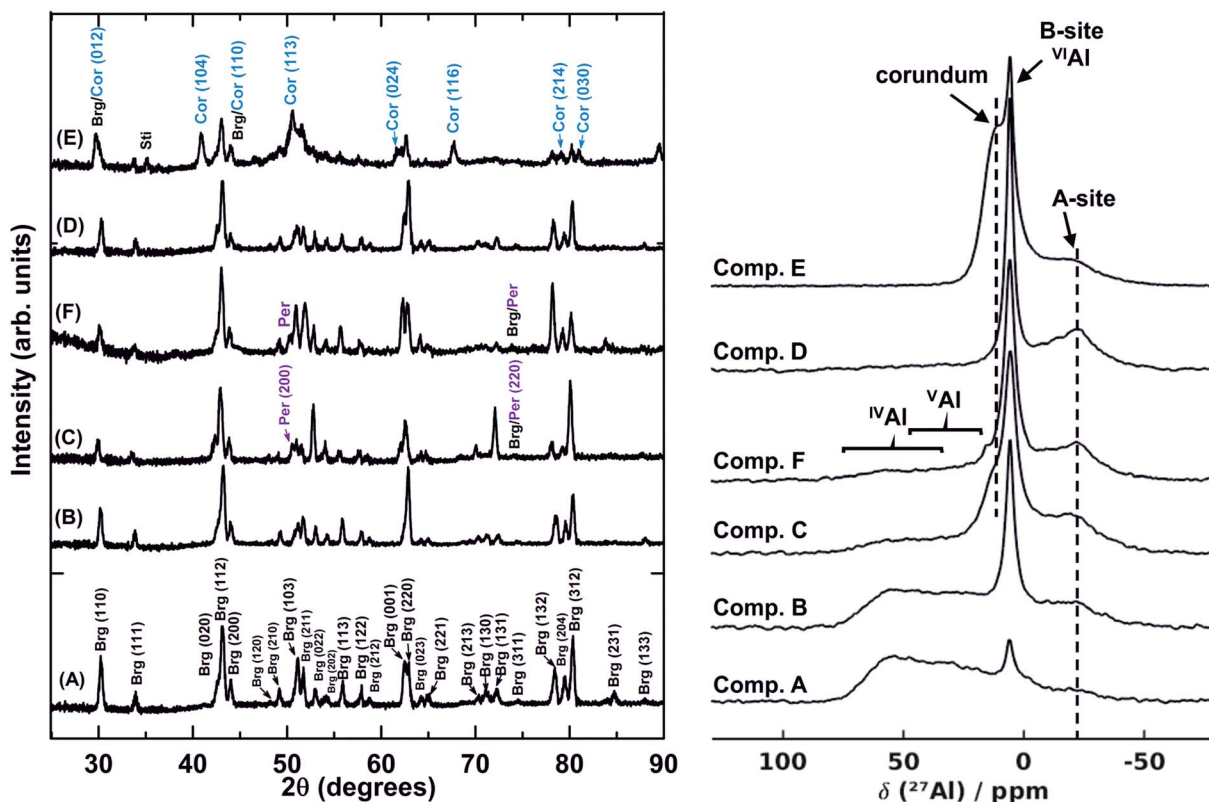


**Figure 1.** X-ray diffraction patterns (left) and <sup>27</sup>Al magic angle spinning (MAS) nuclear magnetic resonance (NMR; right) spectra of Al-bearing bridgmanite samples. (left) All samples are comprised predominantly of bridgmanite (Brg). In samples C and F bridgmanite coexists with periclase (Per) and sample E contains some corundum (Cor). Periclase does not contain any Al and, therefore, does not have an <sup>27</sup>Al NMR spectroscopic signature. (right) All <sup>27</sup>Al MAS NMR spectra exhibit resonances assigned to Al on the A and B sites of bridgmanite. Additionally, the spectra of sample A–C and F exhibit broad resonances in the typical shift range of tetra- (~50–80 ppm) and penta-coordinated (~25–55 ppm) Al species.

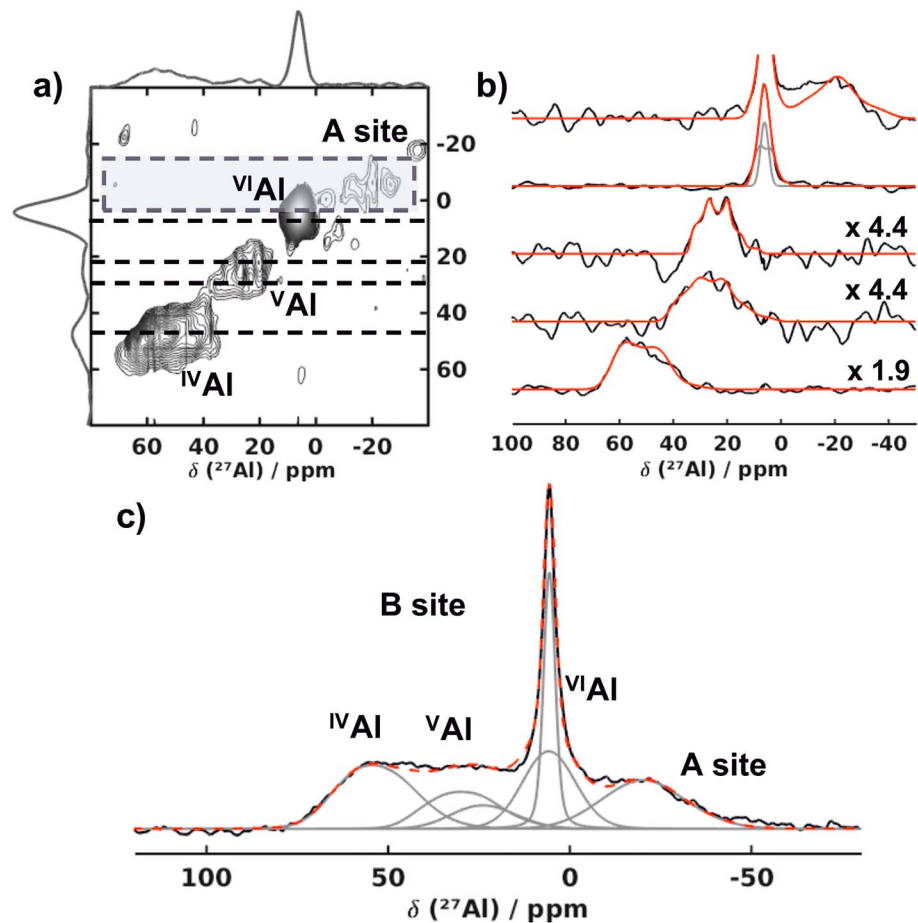


**Figure 2.** (a) Two-dimensional  $^{27}\text{Al}$  satellite-transition magic angle spinning (STMAS) nuclear magnetic resonance (NMR) spectrum, (b) profile fits of the 1-D rows, and (c) resulting refinement of the 1-D  $^{27}\text{Al}$  magic angle spinning (MAS) NMR spectrum of sample B. (a) The 2-D  $^{27}\text{Al}$  STMAS NMR spectrum reveals four distinct Al environments typical for  $\text{IVAl}$ ,  $\text{VAl}$ , and  $\text{VIAl}$  in addition to Al on the A site of bridgmanite ( $\text{Al}$ ). (b) Profile fits (red) of the individual resonances for the 1-D rows indicated by dashed lines and the grey shaded area in (a). Relevant refinement parameters are given in Table S4. (c) Refinement of the corresponding 1-D  $^{27}\text{Al}$  MAS NMR spectrum with resonances for  $\text{IVAl}$ ,  $\text{VAl}$ ,  $\text{VIAl}$ , and  $\text{Al}$ .

signal with a maximum at about  $-20$  ppm, indicating a larger coordination number and a distorted environment for the Al species. In accordance with the literature these signals are assigned to Al on the B and the A site, respectively, (Palke et al., 2012; Stebbins et al., 2001, 2006, 2003) and can be explained by the CC substitution mechanism. The NMR spectra of samples E and C exhibit an additional signal ( $\sim 15$  ppm) corresponding to corundum (Palke et al., 2012; Stebbins et al., 2006), which is consistent with the X-ray diffraction (XRD) phase analysis (Figure 1, left). However, in the spectra of samples A–C and F broad and overlapping resonances in the typical shift range of tetra- and penta-coordinated Al ( $\text{IVAl}$ ,  $\text{VAl}$ ) were observed (Choi et al., 2009; MacKenzie & Smith, 2002; Smith, 1993).

While BSE images and the XRD analysis provide no evidence for the presence of amorphous materials, we cannot rule out the existence of small amounts of glassy materials based on these measurements alone. Previous studies, however, demonstrate the crystallization of  $\text{MgSiO}_3$  glass even at 1100 K (Ono et al., 2017) at similar pressures, so the initial starting material glass must have fully crystallized during the experiment. Although it is possible that minor amounts of  $\text{H}_2\text{O}$  adsorbed onto the starting materials could have induced small degree melting of the sample, such a melt is not expected to be enriched in Al based on measured bridgmanite-melt partition coefficients (Corgne et al., 2005; Liebske et al., 2005), and therefore, the NMR signal would be very weak. Furthermore, such a melt would likely contain  $\text{VIAl}$  rather than  $\text{IVAl}$  and  $\text{VAl}$  species (Allwardt et al., 2005) and would crystallize on quenching. As a consequence we can be

quite certain that the observed  $^{IV}Al$  and  $^{V}Al$  signals are a characteristic feature of Al defects in Al-bearing bridgmanite.

To develop a microscopic understanding of the CC and OV incorporation mechanisms as a function of the synthesis conditions, we extracted the ratios of  $^{IV}Al$ ,  $^{V}Al$ , and  $^{VI}Al$  species and Al on the A site ( $^{A}Al$ ) by a quantitative deconvolution of the  $^{27}Al$  NMR spectra (Table S4 and Figure S3). For this, two reference samples (D and B) were selected in order to assign a characteristic spectral lineshape to each individual Al environment. The EPMA results for sample D imply mainly CC defects (Table 1), and its  $^{27}Al$  NMR spectrum could be refined with two Al resonances typical for Al on the A and B sites (Figure S2), in agreement with previous results (Stebbins et al., 2003, 2006). Both the chemical shift ( $\delta_{iso}$ ) and the quadrupolar coupling interaction ( $C_Q$ ) and asymmetry parameter ( $\eta_Q$ ) show a distribution consistent with disorder of the bond distances, angles, and second-neighbor cations around the Al defects in the bridgmanite structure. The relevant refinement parameters are summarized in Table S4.

The EPMA analyses for sample B indicate that it has the highest stoichiometric OV component (Table 1) and thus offers the best opportunity to identify spectral lineshapes for Al environments influenced by OVs. This was achieved using a 2-D  $^{27}Al$  STMAS spectrum (Figures 2 and Table S4; Ashbrook & Wimperis, 2004; Gan, 2000; Kwak & Gan, 2003), for which four signals were clearly observed. They confirm the presence of the following four Al environments in bridgmanite:  $^{IV}Al$ ,  $^{V}Al$ ,  $^{VI}Al$ , and  $^{A}Al$ . While Al on the A site ( $^{A}Al$ ) results from the CC mechanism,  $^{IV}Al$  and  $^{V}Al$  species are a consequence of neighboring OVs. The  $^{VI}Al$  signal appears to have two contributions, one for the B site substitution associated with the CC mechanism and a broader contribution arising from disorder and distortion introduced by OVs. The entire signal intensity is also too high to be accounted for by CC defects alone. These results are also corroborated by  $^{27}Al$  MAS echo spectra (Figure S4) recorded at a higher magnetic field (23.5 T).

To support the assignment of the  $^{27}Al$  NMR spectra, quantum-mechanical calculations for a number of Al defect models were performed to determine values expected for the NMR parameters  $\delta_{iso}$ ,  $C_Q$  and  $\eta_Q$  (Table S6). For the CC substitution mechanism two defect models were calculated (Figures 3a and 3b), in which one Mg is substituted by Al (A site) and one Si is replaced by Al either at the nearest-neighbor or at the next nearest-neighbor B site (Figures 3a and 3b). For the OV substitution mechanism in total 12 models were considered in order to take into account the possible formation of isolated oxygen vacancies (Figures 3c and S5), as well as the formation of OV dimers (Figures 3d–3f and S6 to S8). Isolated oxygen vacancies shared between two B sites result in the formation of penta-coordinated Al species (Figures 3c and S5), even when clustering linearly on two adjacent octahedra (Figures 3d and S6). However, in order to form tetrahedral  $Al^{3+}$  in the bridgmanite structure, short-range ordering of OVs must occur, as observed, for example, in  $Fe^{3+}$ -bearing  $CaTiO_3$  perovskite (Figures 3e and S7 to S8; Becerro et al., 1999; McCammon et al., 2000). If two neighboring OVs within one octahedron are created, tetrahedral, octahedral, and two pentagonal Al environments are formed (Figure 3e). A further model that was tested is where one Al and one Si occupy the penta-coordinated sites (Figures 3f and S8) and charge balance is maintained by a further Al occupying an octahedral site. In this configuration one  $^{VI}Al$  is not directly associated with the OVs, a possibility that has been proposed previously (Stebbins et al., 2006), which could result, for example, from OV migration. Assuming that combinations of all configurations are possible, for each tetrahedrally coordinated Al either one or two penta-coordinated and octahedral Al sites arise. As a consequence, the intensity ratio cannot be unambiguously linked to one individual configuration for OV short-range order.

The calculated NMR parameters for the CC models (Figures 3a and 3b) are in very good agreement with the experimental values of the signals observed in sample D (Figure 3g). This corroborates the signal assignment of Al on the A and B sites depicted in Figure 2. While CC models including migration of Al within the structure exhibit slightly larger energies ( $\Delta E \sim 10$  kJ/mol), the calculated NMR parameters for all models are quite close to each other (Table S6). As a consequence, we consider both scenarios to be in agreement with the results of the NMR analysis (Figure 3g).

For all considered OV defect models the simulated isotropic chemical shift and quadrupolar coupling constants agree reasonably well with the experimentally obtained values (Figure 3g and Table S6). For the  $^{IV}Al$  species an overestimation of the simulated values of about  $\Delta C_Q = 3$  MHz and  $\Delta \delta_{iso} = 10$  ppm occurred, which we attribute to stronger distortions in the simulations (0 K and ambient pressure), the tendency of

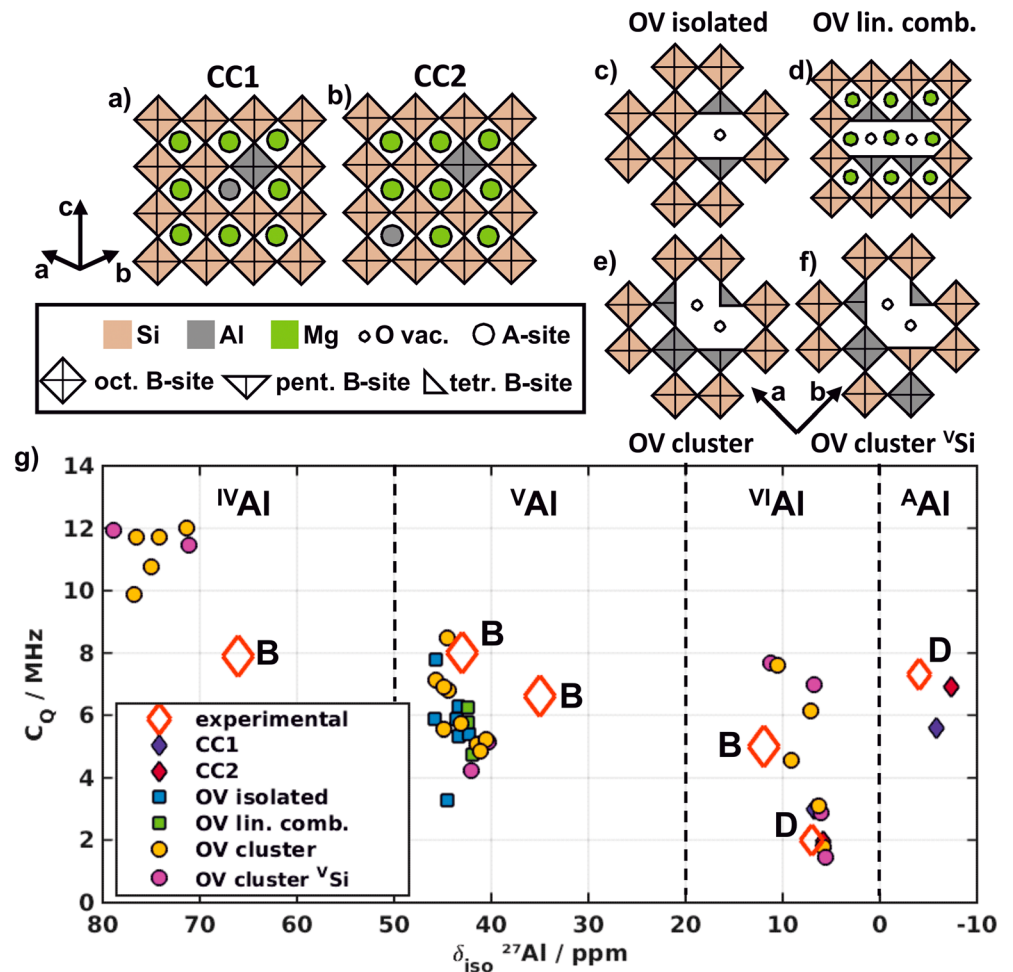


**Figure 3.** (a–f) Schematic representations of Al defect models within bridgmanite and (g) corresponding calculated nuclear magnetic resonance parameters in comparison to the experimental observations. Examples of potential Al defect structures in bridgmanite for the charge coupled (CC; a, b) and the oxygen vacancy (OV) mechanism (c–f) and (g) corresponding calculated quadrupolar coupling  $C_Q$  and isotropic chemical shift  $\delta_{iso}$  of the Al defect sites in comparison to the experimental results of sample B and D. A detailed description of each Al defect model is given in the supporting information.

DFT calculations to overestimate the electric field gradient tensor (Martineau et al., 2014) and to the observed distributions for the chemical shift and quadrupolar coupling values (Table S4).

In particular, the occurrence of tetrahedrally coordinated Al demonstrates the presence of OV clusters comparable to Figures 3e and 3f due to short-range ordering. In the case of the octahedral Al environments, the NMR parameters of those defects not directly associated with OVs fit the experimental data slightly better. This supports the migration of OVs and is potentially consistent with a high mobility of oxygen ions at the synthesis conditions. As a consequence, they exhibit a very similar spectral signature compared to octahedral sites created by the CC substitution mechanism.

#### 4. Discussion

The 1-D <sup>27</sup>Al MAS NMR spectra were deconvoluted using the characteristic parameters for each type of Al coordination (Table 2 and Figure S3), to obtain the relative intensities of each Al environment (Table S5). We use the relative integral of the A site resonance as a measure for Al incorporated due to the CC mechanism, since it is well separated from the other resonances. The same relative intensity is then subtracted from the total <sup>VI</sup>Al intensity according to the stoichiometry of the CC mechanism. The remaining <sup>VI</sup>Al intensity is

**Table 2**  
Quantities (in %) of the  $^{IV}Al$ ,  $^VAl$ ,  $^{VI}Al$ , and  $^AAl$  Species Assigned to the OV Component and the CC Component, Respectively, and Resulting OV/CC (%) Ratio From the 1-D  $^{27}Al$  MAS NMR Spectra

Samples	Al (pfu)	$^{IV}Al$ (%)	$^VAl$ (%)	$^{VI}Al$ (%; OV/CC)	$^AAl$ (%)	OV/CC NMR	OV/CC EPMA
A	0.050	44	23	12/11	11	79 (2)/21 (2)	78 (7)/22 (7)
B	0.100	22	21	17/20	20	60 (3)/40 (3)	67 (4)/33 (4)
C	0.161	9	9	23/29	29	41 (3)/59 (3)	36 (6)/64 (8)
D	0.101	2	3	5/45	45	10 (4)/90 (4)	9 (12)/91 (11)
E	0.235	—	—	—/50	50	0 (2)/100 (2)	2 (4)/98 (5)
F	0.099	10	9	22/30	30	41 (2)/59 (2)	49 (8)/51 (7)

*Note.* The oxygen vacancy (OV)/charge coupled (CC) ratio obtained from the chemical compositions is reported for comparison. MAS = magic angle spinning; NMR = nuclear magnetic resonance.

then combined with the intensities of  $^VAl$  and  $^{IV}Al$  to determine the relative proportion of the OV component. The resulting OV/CC ratios are in good agreement with those estimated from compositional analyses (Table 2), within the analytical uncertainties.

The OV substitution mechanism initially dominates in Al-bearing bridgmanites coexisting with MgO along the  $MgSiO_3$ - $MgAlO_{2.5}$  join and increases with Al content to a maximum in OV component at  $\sim 0.1$  Al pfu (Figure 4a and Table S5), after which the CC substitution, which also increases with increasing Al content, becomes dominant. The presence of  $^{IV}Al$ , even in the lowest Al-bearing sample, however, indicates that there must be partial ordering of OVs, to a degree which appears to decrease with increasing Al-content (Figure 4b, grey and Table S5). The absolute concentrations of  $^{IV}Al$  and  $^VAl$ , however, remain relatively constant up to sample C ( $\sim 0.1$  Al pfu), implying a similar level of partial ordering is maintained until the CC mechanism starts to take over.

Bridgmanites synthesized with coexisting corundum along the  $MgSiO_3$ - $Al_2O_3$  join have a limited OV component and are instead dominated by the CC mechanism (Figure 4a). Note that the bridgmanite sample F contains a significantly higher OV component than sample D, which was produced from the same nominal composition in the absence of excess MgO. This clearly demonstrates that the presence of MgO favors the OV substitution mechanism as it buffers the  $SiO_2$  activity at the lowest level. In a peridotite composition lower mantle, bridgmanite coexists with MgO-rich ferropericlase and the OV mechanism should, therefore, dominate. Although bridgmanite in the lower mantle is expected to contain some  $Fe^{3+}$ , which occupies the A-site

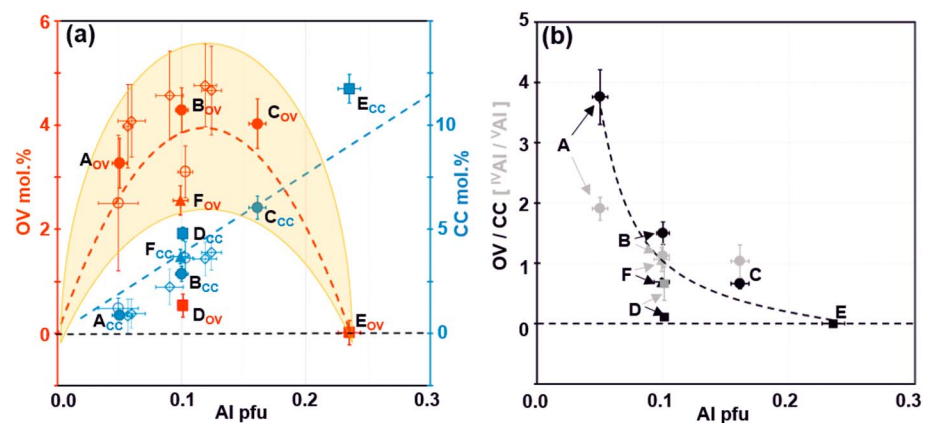


**Figure 4.** (a) Proportions of oxygen vacancy (OV) and charge coupled (CC) components and (b) OV/CC ratio determined by nuclear magnetic resonance spectroscopy. (a) Proportions of OV and CC substituted Al versus Al content (per formula unit) in bridgmanite in the systems  $MgSiO_3$ - $MgAlO_{2.5}$  (circles) and  $MgSiO_3$ - $Al_2O_3$  (squares) and in the reversal run F (triangle), in the present and previous studies. Solid symbols are the present study (Table S5), while the open circle and diamond symbols are data based on analyses of chemical composition from Kojitani et al. (2007) and Navrotsky et al. (2003). The yellow shading outlines the compositional range of the OV component. (b) Additionally to the OV/CC ratio (black) the  $^{IV}Al/^{V}Al$  ratio (grey) determined from the refinement of the 1-D  $^{27}Al$  magic angle spinning nuclear magnetic resonance spectra (Table S5) of sample A to D is depicted.

and forms a stable CC mechanism with  $^{VI}Al$ , the proportion of  $Fe^{3+}$  should be insufficient to balance all Al in this way (Frost et al., 2004; Shim et al., 2017), and compositional evidence indicates that OVs are also present in Fe- and Al-bearing bridgmanite (Frost & Langenhorst, 2002; Lauterbach et al., 2000).

When bridgmanite forms in down welling peridotite material at the top of the lower mantle, it will contain little Al, which partitions strongly into coexisting majoritic garnet at these conditions (Irifune, 1994). With increasing depth, garnet breaks down and the Al content of bridgmanite increases. At depths of approximately 720 km, the OV component in bridgmanite should reach a maximum, but it appears that with a further increase in pressure the OV mechanism becomes less favorable (Brodholt, 2000), and compositional analyses infer that it reaches negligible proportions at depths below 1,000 km (Liu, Ishii, et al., 2017; Liu, Nishi, et al., 2017). In contrast, in basaltic segments of subducting slabs the larger  $Al_2O_3$  content with respect to the ambient mantle will suppress OV formation and favor the CC mechanism for bridgmanite Al substitution. As the formation of OVs is compositionally dependent, lateral variations in their concentration and state of ordering can be expected in the top of the lower mantle, in addition to a gradual decline between depths of 800 to 1,000 km.

A number of transport properties in addition to the partitioning of  $H_2O$  and noble gases are likely linked to the abundance of OVs and their local ordering. Studies of ceramic perovskites have shown that the structural arrangement of OVs have important effects on transport properties. Based on measurements made on the analogous perovskite  $LaAlO_3$ , it has been proposed that the motion of twin domain walls could be a source of seismic wave attenuation in the lower mantle (Harrison & Redfern, 2002). Twin domains, however, were found to become pinned at low temperatures, which was postulated to be caused by OVs that migrate to the twin domain walls. Computer simulations have confirmed that it is energetically favorable for OVs to reside in twin walls (Calleja et al., 2003), raising the intriguing possibility that the partial ordering observed in this study might arise from OV clusters that have migrated to the walls of twin domains, as similar multiple twins are also observed in bridgmanite (Wang et al., 1992). Seismic attenuation in the lower mantle may therefore depend critically on the occurrence of clustered OVs. Similarly, measurements of electrical and ionic conductivity in analogous  $CaTiO_3$ - $CaFeO_{2.5}$  perovskites have been shown to be strongly dependent on the extent of partial ordering of OVs, because it is coupled to an overall decrease in oxygen mobility (Figueiredo et al., 2003; Zhang & Smyth, 1995). Lateral variability in electrical conductivity inferred for the top of the lower mantle (Deschamps, 2015) might, therefore, be explained by compositionally driven variations in OV concentration and ordering.

Previous studies have proposed that noble gases such as neon and argon, which have relatively high solubilities in bridgmanite, may be accommodated on OV sites, due to their comparable atomic size (Shcheka & Keppler, 2012; Zhang & Xu, 1995). This may well be facilitated by the much larger cavity and consequent relaxation resulting from OV partial ordering. It has also been proposed that OVs may be suitable sites for substitution by hydroxyl groups and the possibility has been raised that rapid proton migration could lead to a homogenization of the  $H_2O$  content within the lower mantle (Murakami et al., 2012; Navrotsky, 1999). OV partial ordering, particularly if it occurs within twin domain walls, may have an important effect on proton mobility.

A broad range of lower mantle geochemical and transport properties are, therefore, likely to be dependent on the occurrence and partial ordering of OVs, which may lead to strong variations in physical properties within the top 300 km of the lower mantle. This may even be consistent with the increase in mantle viscosity inferred by some models toward the midlower mantle (Ricard & Wuming, 1991). Numerous studies that have examined bridgmanite physical properties in the past have neglected to buffer the  $SiO_2$  activity and are therefore unlikely to have stabilized OVs in abundances that are realistic for the mantle. Further experiments that pay attention to the role of OV and their local ordering are therefore essential if accurate lower mantle physical and chemical properties are to be determined.

## References

- Allwardt, J. R., Stebbins, J. F., Schmidt, B. C., Frost, D. J., Withers, A. C., & Hirschmann, M. M. (2005). Aluminum coordination and the densification of high-pressure aluminosilicate glasses. *American Mineralogist*, *90*(7), 1218–1222. <https://doi.org/10.2138/am.2005.1836>
- Andraut, D., Neuville, D. R., Flank, A. M., & Wang, Y. (1998). Cation sites in Al-rich  $MgSiO_3$  perovskites. *American Mineralogist*, *83*(9–10), 1045–1053. <https://doi.org/10.2138/am-1998-9-1013>

## Acknowledgments

H. G. acknowledges the “Fonds der Chemischen Industrie” for financial support in the form of the Chemiefonds Fellowship. T.K. acknowledges European Research Council advanced grant No. 787527. All data, including defect models (CIF files), can be found within the manuscript or the supporting information. H. G., Z. L., T. B. B., J. S., and D. J. F. conceived the study; Z. L. was involved with the high-pressure synthesis, as well as the XRD and EPMA analysis of the samples; H. G. and R. S. performed the solid-state NMR experiments; H. G. conceived and conducted the DFT simulations; all authors analyzed and interpreted the data; and H. G., Z. L., T. B. B., J. S., and D. J. F. prepared the manuscript. All authors discussed the results and commented on the manuscript.



- Ashbrook, S. E., & Wimperis, S. (2004). High-resolution NMR of quadrupolar nuclei in solids: the satellite-transition magic angle spinning (STMAS) experiment. *Progress in Nuclear Magnetic Resonance Spectroscopy*, 45(1–2), 53–108. <https://doi.org/10.1016/j.pnmrs.2004.04.002>
- Becerro, A. I., McCammon, C., Langenhorst, F., Seifert, F., & Angel, R. (1999). Oxygen vacancy ordering in  $\text{CaTiO}_3\text{-CaFeO}_{2.5}$  perovskites: From isolated defects to infinite sheets. *Phase Transitions*, 69(1), 133–146. <https://doi.org/10.1080/01411599908208014>
- Bolfan-Casanova, N., Keppler, H., & Rubie, D. C. (2000). Water partitioning between nominally anhydrous minerals in the  $\text{MgO-SiO}_2\text{-H}_2\text{O}$  system up to 24 GPa: Implications for the distribution of water in the Earth's mantle. *Earth and Planetary Science Letters*, 182(3–4), 209–221. [https://doi.org/10.1016/S0012-821X\(00\)00244-2](https://doi.org/10.1016/S0012-821X(00)00244-2)
- Brodholt, J. P. (2000). Pressure-induced changes in the compression mechanism of aluminous perovskite in the Earth's mantle. *Nature*, 407(6804), 620–622. <https://doi.org/10.1038/35036565>
- Calleja, M., Dove, M. T., & Salje, E. K. H. (2003). Trapping of oxygen vacancies on twin walls of  $\text{CaTiO}_3$ : A computer simulation study. *Journal of Physics: Condensed Matter*, 15(14), 2301–2307. <https://doi.org/10.1088/0953-8984/15/14/305>
- Charpentier, T. (2011). The PAW/GIPAW approach for computing NMR parameters: A new dimension added to NMR study of solids. *Solid State Nuclear Magnetic Resonance*, 40(1), 1–20. <https://doi.org/10.1016/j.snmr.2011.04.006>
- Choi, M., Matsunaga, K., Oba, F., & Tanaka, I. (2009).  $^{27}\text{Al}$  NMR chemical shifts in oxide crystals: A first-principles study. *The Journal of Physical Chemistry C*, 113(9), 3869–3873. <https://doi.org/10.1021/jp810484j>
- Clark, S. J., Segall, M. D., Pickard, C. J., Hasnip, P. J., Probert, M. J., Refson, K., & Payne, M. C. (2005). First principles methods using CASTEP. *Zeitschrift für Kristallographie-Crystalline Materials*, 220, 567–570.
- Corgne, A., Liebske, C., Wood, B. J., Rubie, D. C., & Frost, D. J. (2005). Silicate perovskite-melt partitioning of trace elements and geochemical signature of a deep perovskitic reservoir. *Geochimica et Cosmochimica Acta*, 69(2), 485–496. <https://doi.org/10.1016/j.gca.2004.06.041>
- Deschamps, F. (2015). Lower mantle electrical conductivity inferred from probabilistic tomography. *Terrestrial, Atmospheric and Oceanic Sciences*, 26(1), 27–40. <https://doi.org/10.3319/TAO.2014.08.19.03>
- Figueiredo, F., Waerenborgh, J., Kharton, V. V., Näfe, H., & Frade, J. R. (2003). On the relationships between structure, oxygen stoichiometry and ionic conductivity of  $\text{CaTi}_{1-x}\text{Fe}_x\text{O}_{3-5}$  ( $x=0.05, 0.20, 0.40, 0.60$ ). *Solid State Ionics*, 156(3–4), 371–381. [https://doi.org/10.1016/S0167-2738\(02\)00762-2](https://doi.org/10.1016/S0167-2738(02)00762-2)
- Frost, D. J., & Langenhorst, F. (2002). The effect of  $\text{Al}_2\text{O}_3$  on Fe–Mg partitioning between magnesiowüstite and magnesium silicate perovskite. *Earth and Planetary Science Letters*, 199(1–2), 227–241. [https://doi.org/10.1016/S0012-821X\(02\)00558-7](https://doi.org/10.1016/S0012-821X(02)00558-7)
- Frost, D. J., Liebske, C., Langenhorst, F., McCammon, C. A., Trønnes, R. G., & Rubie, D. C. (2004). Experimental evidence for the existence of iron-rich metal in the Earth's lower mantle. *Nature*, 428(6981), 409–412. <https://doi.org/10.1038/nature02413>
- Gan, Z. (2000). Isotropic NMR spectra of half-integer quadrupolar nuclei using satellite transitions and magic-angle spinning. *Journal of the American Chemical Society*, 122(13), 3242–3243. <https://doi.org/10.1021/ja9939791>
- Grimme, S. (2006). Semiempirical GGA-type density functional constructed with a long-range dispersion correction. *Journal of Computational Chemistry*, 27(15), 1787–1799. <https://doi.org/10.1002/jcc.20495>
- Harrison, R. J., & Redfern, S. A. T. (2002). The influence of transformation twins on the seismic-frequency elastic and anelastic properties of perovskite: Dynamical mechanical analysis of single crystal  $\text{LaAlO}_3$ . *Physics of the Earth and Planetary Interiors*, 134(3–4), 253–272. [https://doi.org/10.1016/S0031-9201\(02\)00190-5](https://doi.org/10.1016/S0031-9201(02)00190-5)
- Irfune, T. (1994). Absence of an aluminous phase in the upper part of the Earth's lower mantle. *Nature*, 370(6485), 131–133. <https://doi.org/10.1038/370131a0>
- Ishii, T., Shi, L., Huang, R., Tsujino, N., Druzhbin, D., Myhill, R., et al. (2016). Generation of pressures over 40 GPa using Kawai-type multi-anvil press with tungsten carbide anvils. *Review of Scientific Instruments*, 87(2), 024501. <https://doi.org/10.1063/1.4941716>
- Kentgens, A. P. (1991). Quantitative excitation of half-integer quadrupolar nuclei by a frequency-stepped adiabatic half-passage. *Journal of Magnetic Resonance*, 95(3), 619–625. [https://doi.org/10.1016/0022-2364\(91\)90179-W](https://doi.org/10.1016/0022-2364(91)90179-W)
- Klie, R. F., Ito, Y., Stemmer, S., & Browning, N. D. (2001). Observation of oxygen vacancy ordering and segregation in Perovskite oxides. *Ultramicroscopy*, 86(3–4), 289–302. [https://doi.org/10.1016/S0304-3991\(00\)00120-0](https://doi.org/10.1016/S0304-3991(00)00120-0)
- Kojitani, H., Katsura, T., & Akaogi, M. (2007). Aluminum substitution mechanisms in perovskite-type  $\text{MgSiO}_3$ : an investigation by Rietveld analysis. *Physics and Chemistry of Minerals*, 34(4), 257–267. <https://doi.org/10.1007/s00269-007-0144-z>
- Kruidhof, H., Bouwmeester, H. J. M., Doorn, R. H. E., & Burggraaf, A. J. (1993). Influence of order-disorder transitions on oxygen permeability through selected nonstoichiometric perovskite-type oxides. *Solid State Ionics*, 63–65(02), 816–822. [https://doi.org/10.1016/0167-2738\(93\)90202-E](https://doi.org/10.1016/0167-2738(93)90202-E)
- Kurnosov, A., Marquardt, H., Frost, D. J., Ballaran, T. B., & Ziberna, L. (2017). Evidence for a  $\text{Fe}^{3+}$ -rich pyrolytic lower mantle from (Al,Fe)-bearing bridgmanite elasticity data. *Nature*, 558(7710), E3–E546. <https://doi.org/10.1038/s41586-018-0115-1>
- Kwak, H.-T., & Gan, Z. (2003). Double-quantum filtered STMAS. *Journal of Magnetic Resonance*, 164(2), 369–372. [https://doi.org/10.1016/S1090-7807\(03\)00246-5](https://doi.org/10.1016/S1090-7807(03)00246-5)
- Lauterbach, S., McCammon, C. A., van Aken, P., Langenhorst, F., & Seifert, F. (2000). Mössbauer and ELNES spectroscopy of (Mg,Fe)(Si,Al) $\text{O}_3$  perovskite: A highly oxidised component of the lower mantle. *Contributions to Mineralogy and Petrology*, 138(1), 17–26. <https://doi.org/10.1007/PL00007658>
- Liebske, C., Corgne, A., Frost, D. J., Rubie, D. C., & Wood, B. J. (2005). Compositional effects on element partitioning between Mg-silicate perovskite and silicate melts. *Contributions to Mineralogy and Petrology*, 149(1), 113–128. <https://doi.org/10.1007/s00410-004-0641-8>
- Liu, Z., Akaogi, M., & Katsura, T. (2019). Increase of the oxygen vacancy component in bridgmanite with temperature. *Earth and Planetary Science Letters*, 505, 141–151. <https://doi.org/10.1016/j.epsl.2018.10.014>
- Liu, Z., Ishii, T., & Katsura, T. (2017). Rapid decrease of  $\text{MgAlO}_{2.5}$  component in bridgmanite with pressure. *Geochemical Perspectives Letters*, 5, 12–18. <https://doi.org/10.7185/geochemlet.1739>
- Liu, Z., Nishi, M., Ishii, T., Fei, H., Miyajima, N., Ballaran, T. B., et al. (2017). Phase relations in the system  $\text{MgSiO}_3\text{-Al}_2\text{O}_3$  up to 2300 K at lower mantle pressures. *Journal of Geophysical Research: Solid Earth*, 122, 7775–7788. <https://doi.org/10.1002/2017JB014579>
- MacKenzie, K. J. D., & Smith, M. E. (2002). In R. W. Kahn (Ed.), *Multinuclear solid-state NMR of inorganic materials*, Pergamon Materials Series, (Vol. 6). Oxford: Pergamon Press.
- Manthilake, G. M., de Koker, N., Frost, D. J., & McCammon, C. A. (2011). Lattice thermal conductivity of lower mantle minerals and heat flux from Earth's core. *Proceedings of the National Academy of Sciences*, 108(44), 17,901–17,904. <https://doi.org/10.1073/pnas.1110594108>
- Martineau, C., Senker, J., & Taulelle, F. (2014). NMR crystallography. *Annual Reports on NMR Spectroscopy*, 82, 1–57. <https://doi.org/10.1016/B978-0-12-800184-4.00001-1>

- McCammon, C. (1997). Perovskite as a possible sink for ferric iron in the lower mantle. *Nature*, *387*(6634), 694–696. <https://doi.org/10.1038/42685>
- McCammon, C. A., Becerro, A. I., Langenhorst, F., Angel, R. J., Marion, S., & Seifert, F. (2000). Short-range ordering of oxygen vacancies in  $\text{CaFe}_x\text{Ti}_{1-x}\text{O}_{3-x/2}$  perovskites ( $0 < x < 0.4$ ). *Journal of Physics: Condensed Matter*, *12*(13), 2969–2984. <https://doi.org/10.1088/0953-8984/12/13/308>
- Murakami, M., Ohishi, Y., Hirao, N., & Hirose, K. (2012). A perovskitic lower mantle inferred from high-pressure, high-temperature sound velocity data. *Nature*, *485*(7396), 90–94. <https://doi.org/10.1038/nature11004>
- Navrotsky, A. (1999). A lesson from ceramics. *Science*, *284*(5421), 1788–1789. <https://doi.org/10.1126/science.284.5421.1788>
- Navrotsky, A., Schoenitz, M., Kojitani, H., Xu, H., Zhang, J., Weidner, D. J., & Jeanloz, R. (2003). Aluminum in magnesium silicate perovskite: Formation, structure, and energetics of magnesium-rich defect solid solutions. *Journal of Geophysical Research*, *108*(B7), 2330. <https://doi.org/10.1029/2002JB002055>
- Ono, S., Kikegawa, T., & Higo, Y. (2017). Reaction boundary between akimotoite and ringwoodite + stishovite in  $\text{MgSiO}_3$ . *Physics and Chemistry of Minerals*, *44*(6), 425–430. <https://doi.org/10.1007/s00269-016-0869-7>
- Palke, A. C., Stebbins, J. F., Frost, D. J., & McCammon, C. A. (2012). Incorporation of Fe and Al in  $\text{MgSiO}_3$  perovskite: An investigation by  $^{27}\text{Al}$  and  $^{29}\text{Si}$  NMR spectroscopy. *American Mineralogist*, *97*(11–12), 1955–1964. <https://doi.org/10.2138/am.2012.4101>
- Perdew, J. P., Burke, K., & Ernzerhof, M. (1996). Generalized gradient approximation made simple. *Physical Review Letters*, *77*(18), 3865–3868. <https://doi.org/10.1103/PhysRevLett.77.3865>
- Pickard, C., & Mauri, F. (2001). All-electron magnetic response with pseudopotentials: NMR chemical shifts. *Physical Review B*, *63*(24), 245101. <https://doi.org/10.1103/PhysRevB.63.245101>
- Profeta, M., Mauri, F., & Pickard, C. J. (2003). Accurate first principles prediction of  $^{17}\text{O}$  NMR parameters in  $\text{SiO}_2$ : Assignment of the zeolite ferrierite spectrum. *Journal of the American Chemical Society*, *125*(2), 541–548. <https://doi.org/10.1021/ja027124r>
- Ricard, Y., & Wuming, B. (1991). Inferring the viscosity and the 3-D density structure of the mantle from geoid, topography and plate velocities. *Geophysical Journal International*, *105*(3), 561–571. <https://doi.org/10.1111/j.1365-246X.1991.tb00796.x>
- Shcheka, S. S., & Kepler, H. (2012). The origin of the terrestrial noble-gas signature. *Nature*, *490*(7421), 531–534. <https://doi.org/10.1038/nature11506>
- Shim, S.-H., Grocholski, B., Ye, Y., Alp, E. E., Xu, S., Morgan, D., et al. (2017). Stability of ferrous-iron-rich bridgmanite under reducing midmantle conditions. *Proceedings of the National Academy of Sciences*, *114*(25), 6468–6473. <https://doi.org/10.1073/pnas.1614036114>
- Siegel, R., Rocha, J., & Mafra, L. (2009). Combining STMAS and CRAMPS NMR spectroscopy: High-resolution HETCOR NMR spectra of quadrupolar and 1H nuclei in solids. *Chemical Physics Letters*, *470*(4–6), 337–341. <https://doi.org/10.1016/j.cplett.2009.01.053>
- Smith, M. E. (1993). Application of  $^{27}\text{Al}$  NMR techniques to structure determination in solids. *Applied Magnetic Resonance*, *4*(1–2), 1–64. <https://doi.org/10.1007/BF03162555>
- Stebbins, J. F., Du, L.-S., Kelsey, K., Kojitani, H., Akaogi, M., & Ono, S. (2006). Aluminum substitution in stishovite and  $\text{MgSiO}_3$  perovskite: High-resolution  $^{27}\text{Al}$  NMR. *American Mineralogist*, *91*(2–3), 337–343. <https://doi.org/10.2138/am.2006.1988>
- Stebbins, J. F., Kojitani, H., Akaogi, M., & Navrotsky, A. (2003). Aluminum substitution in  $\text{MgSiO}_3$  perovskite: Investigation of multiple mechanisms by  $^{27}\text{Al}$  NMR. *American Mineralogist*, *88*(7), 1161–1164. <https://doi.org/10.2138/am-2003-0724>
- Stebbins, J. F., Kroeker, S., & Andrault, D. (2001). The mechanism of solution of aluminum oxide in  $\text{MgSiO}_3$  perovskite. *Geophysical Research Letters*, *28*(4), 615–618. <https://doi.org/10.1029/2000GL012279>
- Wang, Y., Guyot, F., & Liebermann, R. C. (1992). Electron microscopy of  $(\text{Mg, Fe})\text{SiO}_3$  Perovskite: Evidence for structural phase transitions and implications for the lower mantle. *Journal of Geophysical Research*, *97*(B9), 12,327. <https://doi.org/10.1029/92JB00870>
- Xu, Y., & McCammon, C. (2002). Evidence for ionic conductivity in lower mantle  $(\text{Mg, Fe})(\text{Si, Al})\text{O}_3$  perovskite. *Journal of Geophysical Research*, *107*(B10), 2251. <https://doi.org/10.1029/2001JB000677>
- Yates, J. R., Pickard, C. J., & Mauri, F. (2007). Calculation of NMR chemical shifts for extended systems using ultrasoft pseudopotentials. *Physical Review B*, *76*(2), 24,401. <https://doi.org/10.1103/PhysRevB.76.024401>
- Zhang, G. B., & Smyth, D. M. (1995). Defects and transport of the brownmillerite oxides with high oxygen ion conductivity— $\text{Ba}_2\text{In}_2\text{O}_5$ . *Solid State Ionics*, *82*(3–4), 161–172. [https://doi.org/10.1016/0167-2738\(95\)00196-2](https://doi.org/10.1016/0167-2738(95)00196-2)
- Zhang, Y., & Xu, Z. (1995). Atomic radii of noble gas elements in condensed phases. *American Mineralogist*, *80*(7–8), 670–675. <https://doi.org/10.2138/am-1995-7-803>